The 9th European Congress on Computational Methods in Applied Sciences and Engineering
ECCOMAS Congress 2024
3 – 7 June 2024, Lisboa, Portugal

NUMERICAL INVESTIGATION OF ELECTROSTATIC COATING USING NITROTHERM SPRAY TECHNIQUE

A. BENMOUSSA[*], M. R. PENDAR[†] AND J. PASCOA[*]

[*] Center for Mechanical and Aerospace Science and Technologies
(C-MAST), University of Beira Interior
Rua Marquês D'Ávila e Bolama, 6201-001 Covilhã, Portugal
e-mail: amine.benmoussa@ubi.pt, pascoa@ubi.pt

[†] Department of Mechanical Engineering, University of Victoria
British Columbia V8W2Y2 Victoria, Canada
email: pendar@uvic.ca

Key words: Nitrotherm Electrostatic Spray, Large Eddy Simulation (LES), OpenFOAM, Droplets Electrical Charging.

Summary. *In this study, a 3D Eulerian-Lagrangian algorithm is employed to evaluate the Nitrotherm electrostatic spray technique, with the goal of optimizing transfer efficiency and enhancing painting performance. The fluid dynamics are simulated by solving the unsteady 3D compressible Navier-Stokes equations, while particle motion is modeled by tracking the distribution of droplet sizes. Implemented within the OpenFOAM framework, the algorithm incorporates a Large Eddy Simulation (LES) turbulence model to capture the high Reynolds number airflow. Additionally, it includes detailed simulations of spray dynamics, electric fields, and droplet trajectories. The findings suggest that using heated nitrogen-enriched air, instead of compressed air, reduces paint consumption and improves transfer efficiency (TE). The Nitrotherm technique also decreases application time by leveraging the low temperature of pure nitrogen for quicker curing, evaporation, and drying, resulting in a higher-quality paint film. This approach contributes to producing a superior cosmetic paint finish on the target and minimizes overspray, leading to a notably thicker film compared to conventional methods using compressed air.*

1 INTRODUCTION

As industries continue to prioritize efficiency and sustainability in coating processes, advancements in spray painting technology have become increasingly significant. Conventional spray-painting technologies, despite their widespread use, are often hampered by limitations such as high paint waste, substantial volatile organic compound (VOC) emissions, and extended application times [1]. These challenges not only affect operational costs but also contribute to environmental pollution. To address these concerns, advancements in coating technologies are necessary, with recent developments focusing on electrostatic spray techniques and innovative methods such as the Nitrotherm spray technique.

Electrostatic spray coating has been recognized for its ability to enhance transfer efficiency by utilizing an electric field to attract paint particles to the target surface, thus reducing

overspray and paint waste. Recent research has significantly advanced the understanding of electrostatic spray technology, offering deeper insights into spray deposition and efficiency, such as droplet transport during spraying and the resulting film thickness [2], electrical space charge [3], wall film dynamics [4], droplet size distributions [5], and the influence of airflow shaping [6].

Pendar et al. [7, 8] conducted a numerical study to evaluate flowfield characteristics and particle distribution during coating, they highlighted the significant impact of voltage and external conductors on the electrostatic spraying process. Im et al. [9] performed a computational fluid dynamics (CFD) study on the transfer process during electrostatic spraying using a rotary bell sprayer. Their study revealed that the charge-to-mass ratio, electric force, and transfer efficiency are highly sensitive to the spray shape. They also discovered that increasing the shaping airflow could lead to a decrease in transfer efficiency, underscoring the delicate balance required in optimizing airflow and spray characteristics. Colbert et al. [10] conducted parametric studies on electrostatic sprayers and observed that the accumulation of spray material was notably higher at the edges of the target when employing a ring model, with minimal deposition at the center of a flat target. This finding highlights the challenges in achieving uniform coating when using traditional spray patterns. Ye et al. [11] utilized CFD FLUENT software to simulate a complex spray gun incorporating a corona charge mechanism. Their simulation, which compared actual particle sizes and charge amounts with experimental data, demonstrated the significant impact of space charge on deposition thickness on a stationary plate. This study highlights the importance of accurate simulation parameters in understanding the electrostatic effects on coating uniformity. Krisshna et al. [12] employed computational simulations to investigate three-dimensional near-bell atomization. By incorporating electrohydrodynamic (EHD) effects, their study revealed that smaller droplets were generated, with minimal impact on primary atomization. Shen et al. [13] investigated the phenomena of droplet disintegration and the behavior of non-Newtonian fluids [14, 15] when applied as input paint in high-speed rotary bell atomizers.

These studies have significantly advanced our understanding of the effects of electric fields on droplet characteristics and electrostatic coating processes [16]. However, conventional systems still face inefficiencies related to air-based paint delivery, leading to suboptimal coverage and increased VOC emissions. The Nitrotherm spray technique addresses these issues by using heated, nitrogen-enriched gas instead of compressed air, resulting in improved paint transfer efficiency and reduced environmental impact. The use of heated nitrogen in electrostatic spraying has been explored by a few high-tech companies with promising results. Spang [17] compared spray coating with heated nitrogen to conventional air spraying, reporting improvements in transfer efficiency (TE) and faster paint curing times. Similarly, Bensalah et al. [18] observed higher transfer efficiency with the Nitrotherm coating method, indicating potential reductions in energy and material consumption in paint shops.

In the current study, a 3D Eulerian-Lagrangian evaluation of electrostatic spraying using the Nitrotherm approach was implemented. The algorithm, executed within the OpenFOAM framework, models high Reynolds number airflow through a Large Eddy Simulation (LES) turbulence approach and incorporates spray dynamics, electric field modeling, and droplet tracking for accurate spray coating simulations.

2 GOVERNING EQUATIONS

2.1 Continuous Phase

The flow field is modeled using compressible Navier-Stokes equations with an LES turbulence model, which resolves large, energy-rich eddies and captures smaller sub-grid scales through Favre-averaged continuity and momentum equations. In the LES turbulence model, each variable f' is decomposed into grid scale (GS) and sub-grid scale (SGS) components, such that $\bar{f} = G * f$, where $G = G(X, \Delta)$ is the filter function and $\Delta = \Delta(X)$ is the filter width [19]. The filtered Navier–Stokes equations are given by:

$$\frac{\partial \bar{\rho}}{\partial t} + \frac{\partial (\bar{\rho} \bar{u}_j)}{\partial x_j} = 0, \tag{1}$$

$$\frac{\partial (\bar{\rho} \bar{u}_j)}{\partial t} + \frac{\partial (\bar{\rho} \bar{u}_i \bar{u}_j)}{\partial x_j} = -\frac{\partial \bar{p}}{\partial x_i} + \frac{\partial \bar{\sigma}_{ij}}{\partial x_j} - \frac{\partial \tau_{ij}}{\partial x_j} + f_{st} + f_{es} + S. \tag{2}$$

, where p and $\tilde{\sigma}_{ij}$ denote the pressure and the viscous stress tensor, and is given by:

$$\tilde{\sigma}_{ij} = \bar{\mu} \left(\frac{\partial \tilde{u}_i}{\partial x_j} + \frac{\partial \tilde{u}_j}{\partial x_i} - \frac{2}{3} \delta_{ij} \frac{\partial \tilde{u}_k}{\partial x_k} \right), \tag{3}$$

Where $\bar{\mu}$ denotes the kinematic viscosity, and δ_{ij} represents the Kronecker delta function. The body forces, which encompass electric stress (f_{es}), surface tension (f_{st}) and gravity (S) are incorporated into the aforementioned equations to account for additional physical effects.
The unresolved transport element in the momentum equation, i.e., the SGS stress tensor, τ_{ij}, can be decomposed as [20, 21]:

$$\tau_{ij} \approx \bar{\rho} (\overline{u_i u_j} - \overline{u_i}\,\overline{u_j}) , \tag{4}$$

2.2 Electric Field

The electric field is generated by the potential difference between the highly negatively charged surfaces of the sprayer and the positively charged target, and is described by Poisson's equation, which relates the space charge density (ρ^q) caused by to the ions to the potential (φ), and given by:

$$\nabla^2 \phi = -\frac{\rho^q}{\varepsilon'} . \tag{5}$$

The electric field ($\vec{E}$) and charge of each particle (Q) are calculated by:

$$\vec{E} = -\nabla \phi , \ \varepsilon' \nabla . E = \rho^q , \tag{6}$$

$$Q_i = m_{P_i} \rho^{\mathrm{q}}_{\mathrm{m_i}} = (\rho_P V_{P_i}) \rho^{\mathrm{q}}_{\mathrm{m_i}} , \tag{7}$$

ε', ρ_P, V_{P_i}, and $\rho^{\mathrm{q}}_{\mathrm{m_i}}$ represent air electrical permittivity, density, volume of each individual particle and charge to mass ratio, respectively. It is important to note that ρ^q and Q have distinct

units, representing charge per unit volume and charge, respectively. The electric force, denoted as (F_E), is calculated as the interaction of the electrical field with the airflow, often referred to as the ion wind, which directly affects the particles and is defined by:

$$F_E = q_{P_i} E = m_{P_i} \rho_m^q E, \tag{8}$$

where m_{P_i} and q_{P_i} are the mass and the charge of each individual droplet, respectively.

2.3 Discrete Phase

The discrete phase analyzes the motion of charged droplets in airflow using a Lagrangian framework. This includes solving differential equations and applying Newton's law for force balances. The forces affecting droplet trajectory—Stokes drag (f_D), electric force (f_E), gravity (f_G), and added-mass effects (f_M), are defined as follows:

$$\vec{F}_P = m_p \frac{\partial \vec{u}_p}{\partial t} = \frac{3}{4} C_d \frac{\rho_f}{\rho_P} \frac{m_P}{2R_P} \left|(\vec{u}_f - \vec{u}_P)\right| (\vec{u}_f - \vec{u}_P) + (\rho_P - \rho_f) V_P \vec{g} + \vec{E} q_P + \frac{\rho_f V_P}{2} \frac{\partial (\vec{u}_f - \vec{u}_p)}{\partial t} \tag{9}$$

Where $\vec{u}_P$ and $\vec{u}_f$ denote the velocity vectors of particles and fluid, ρ_P and ρ_f denote the densities of particles and fluid, respectively. Additionally, q_P, m_P, V_P and R_P correspond to the charge, mass, volume and radius of the particles, respectively.
The drag coefficient (C_D), which depends on the particle's Reynolds number ($\mathrm{Re_p} = 2R_p \left|\vec{u}_f - \vec{u}_p\right| \rho_f / \mu_f$), is given by [22, 23]:

$$C_D = \begin{cases} 24/\mathrm{Re}_P, & if \quad \mathrm{Re}_P < 1 \\ (24/\mathrm{Re}_P)(1 + 0.5\,\mathrm{Re}_P^{0.687}), & if \quad 1 \le \mathrm{Re}_P \le 1000 \\ 0.44, & if \quad \mathrm{Re}_P > 1000 \end{cases} \tag{10}$$

Where $\vec{\mu}_f$ is the dynamic viscosity of the air.

2.4 Breakup Model:

In spraying procedures, breakup modeling is crucial and consists of primary and secondary phases. The primary breakup involves the initial liquid disintegration into droplets as it exits the nozzle, modeled by the Rosin-Rammler distribution ($Y_d = \exp(-d/\bar{d})^n$). For secondary breakup, the modified Taylor Analogy Breakup (TAB) method, using the Weber number ($We = \rho u_{rel}^2 D_P / \sigma$), predicts how parent droplets break into smaller droplets based on the product generation rate $dn(\mathrm{t})/\mathrm{dt}$ and a proportional constant (k_{br}), given by:

$$dn(\mathrm{t})/dt = -3K_{br} n(\mathrm{t}), \quad K_{br} = \begin{cases} k_1 \omega & \text{if} \quad We \le We_t \\ k_2 \omega \sqrt{We} & \text{if} \quad We > We_t \end{cases} \tag{11}$$

Where the transient Weber number (We_t) is set to 100, and k_1 and k_2 are adjusted to match experimental droplet velocity and size ($k_1 \approx k_2 = 0.2$) [8]. The resultant distribution of product droplets is defined as:

$$\frac{r_{product}}{r_{parent}} = e^{-K_{br}t} \tag{12}$$

Where r_{parent} and $r_{product}$ denote the parent and product droplets radius.

2.5 Film Deposition Formulations:

The detailed formulations for mass conservation, momentum, energy, and thickness of the film formed during spray droplet deposition on the target are provided in the authors' previous work [7].

3 SIMULATION METHODOLOGY

3.1 Computational domain and boundary conditions

Figure 1 shows the simplified computational domain of the Nitrotherm electrostatic spray, represented as a cylinder with dimensions 540D and 70D, where D = 2.5 mm is the injection nozzle diameter. To ensure accurate results and fast convergence, the Courant number is kept below 0.45, corresponding to a time step of 1×10−7 s. Atmospheric boundary conditions simulate real conditions, with no-slip walls for the sprayer and the target workpiece. A constant flow rate paint jet with a diameter of D = 2.5 mm is supplied at the sprayer center. The nitrogen/air nozzle uses a velocity inlet, and specific potential values ($\Phi = V_1$) are assigned to the sprayer's body and retaining collar, all made of stainless steel for electric field boundary conditions. The remaining parts of the sprayer, made of non-conductive plastic, are treated with $(\nabla\Phi).\mathrm{n} = 0$. various charge ($\rho^{q}_{m_i}$) values are also assigned to the surfaces of the disintegrated droplets, while potential values for all other boundaries are set $\Phi = 0$.

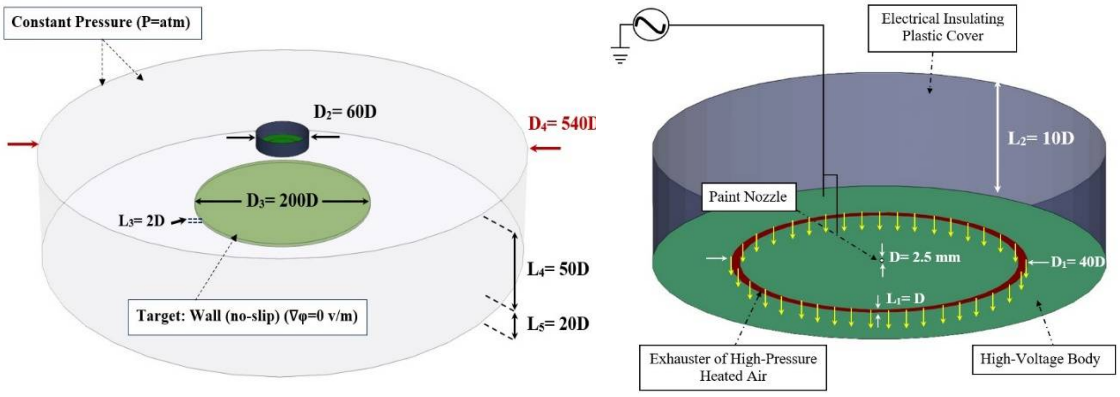

Figure 1: Schematic of the geometry dimensions and boundary conditions for analyzing the Nitrotherm spray technique (a). Close-up view of the sprayer (b).

3.2 Grid representation

Figure 2 presents the generated mesh, where structured quadrilateral meshes were used for the entire domain, consisting of 1.2 million cells. This mesh was found to provide reliable convergence in the authors' grid independence study as reported in [8]. The prism layer height,

set at 1.4×10^{-4} m along solid boundaries, and y^+ values of 0.35, effectively captures high-Reynolds turbulent flow mechanisms, ensuring accurate boundary layer dynamics. Additionally, a mesh sensitivity analysis using the Kolmogorov power law decay ($f^{-5/3}$) validated the mesh's ability to capture detailed turbulent flow structures.

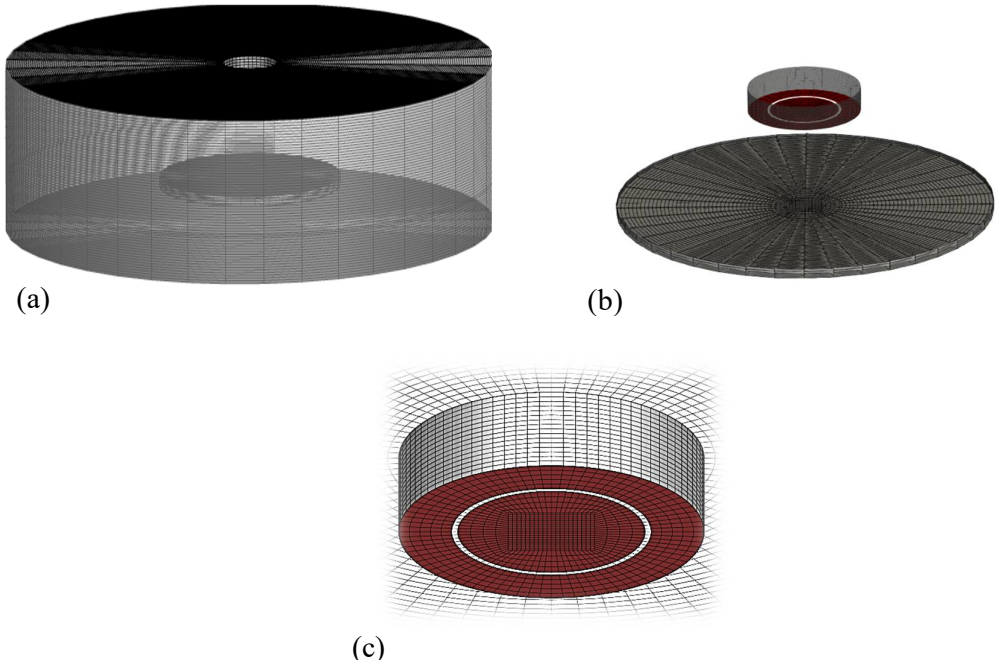

Figure 2: Visualization of the structured grid generated for the specified geometry for electrospray evaluation (a). Detailed view of the nozzle and target area (b). Detailed view of the injection section (c).

3.3 Solver setting

In this study, discretization schemes are employed to achieve precise results, maintaining second-order accuracy for all terms with a convergence criterion set at 1×10^{-6}. The PIMPLE algorithm is employed, combining the PISO and SIMPLE methods, known for its stability and rapid convergence even with larger time steps. The PISO algorithm handles the inner corrector loop, while the SIMPLE algorithm manages the outer loop. In the Eulerian-Lagrangian simulation, wall treatment in LES turbulence modeling within the OpenFOAM framework depends on the dimensionless wall distance ($y^+ = (u_\tau . \Delta y)/\upsilon$), where u_τ denotes the friction velocity, υ represents the kinematic viscosity and Δy is the nearest distance to the wall surface.

4 RESULTS AND DISCUSSION

Figure 3 presents a comparison of the computed dimensionless radial velocity values near the nozzle with the experimental data from Stevenin et al. [6]. These velocity values, normalized by the maximum radial velocity, are extracted from the turbulent boundary layer adjacent to the bell cup surface and extending outward. The simulation demonstrates a high degree of accuracy, with the maximum discrepancy between the numerical and experimental

results being less than 1.5%.

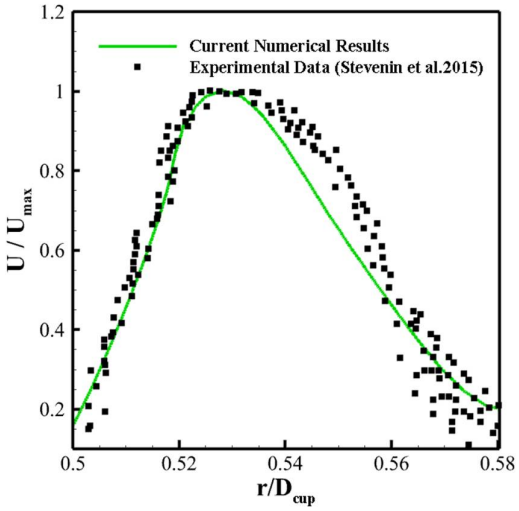

Figure 3: Comparison of radial velocity distribution between our numerical results and experimental data[6].

Figure 4 illustrates the interaction between the injected heated nitrogen, electric fields, and the sprayed droplets as they are emitted from the nozzle and directed toward the target surface. In Figure 4a, the velocity gradient shows higher speeds near the sprayer, decreasing as droplets move away, underscoring the role of the injected nitrogen in shaping the spray. Figure 4b displays the electric potential between the nozzle and target, which influences spray patterns and droplet trajectories to accelerate the transfer process. The absolute value of the negative voltage plays a crucial role in controlling the spray plume.

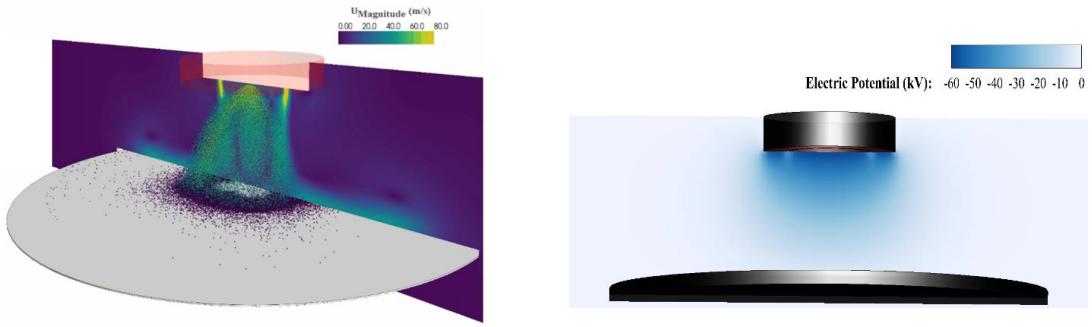

(a) (b)

Figure 4: Injected heated nitrogen with sprayed droplets distribution (a) and electric field distribution (b).

Figure 5 illustrates the effect of injected heated nitrogen velocity on vortical structures using the Line Integral Convolution method (I) and the pattern of deposited spray paint droplets (II). The velocities considered are 0, 150, and 300 m/s. It is evident that the velocity of the injected nitrogen greatly influences the deviation of droplets, the overspray effect, the irregularity of covered area borders, film thickness, and central fill. Increasing the nitrogen injection velocity

optimizes these factors, resulting in denser and thicker finishes with improved transfer efficiency.

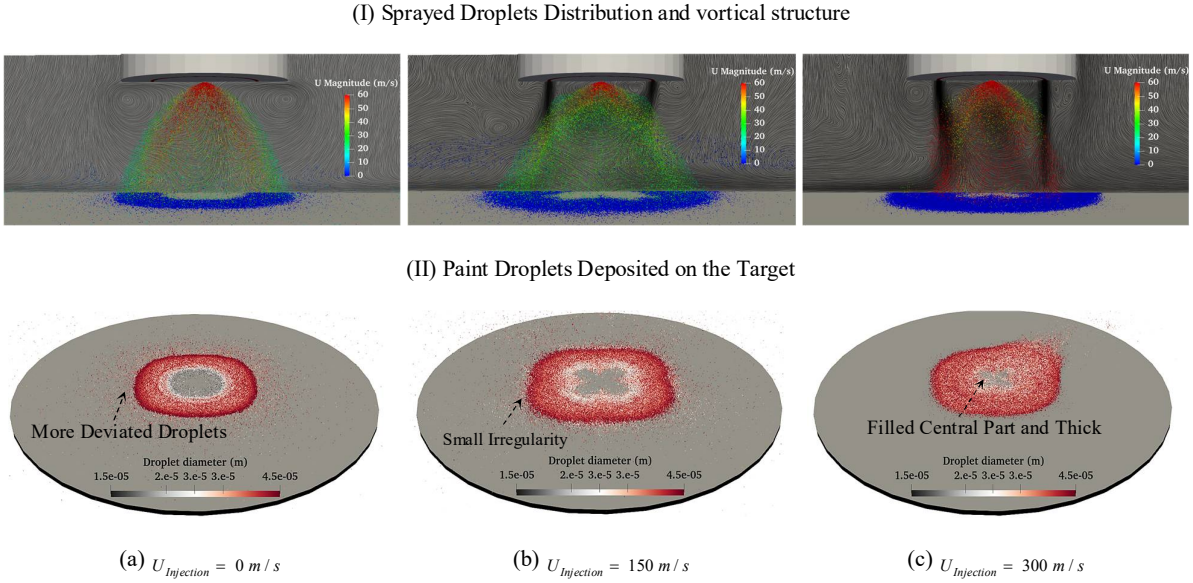

Figure 5: Effect of Heated Nitrogen Injection Velocity on Droplet Trajectory and Deposition Pattern: (a) $U_{Injection} = 0\ m/s$,(b) $U_{Injection} = 150\ m/s$, and (c) $U_{Injection} = 300\ m/s$ ($T_{Nitrogen} = 393.15^{\circ} K$).

As shown in Figure 6, improper force interactions due to smaller sizes result in irregular and tiny wetted areas. The results indicate that a larger droplet size distribution leads to a more uniform and thicker coverage. As the initial droplet size increases, the diameter of the predicted deposited area grows, resulting in a regular and even pattern.

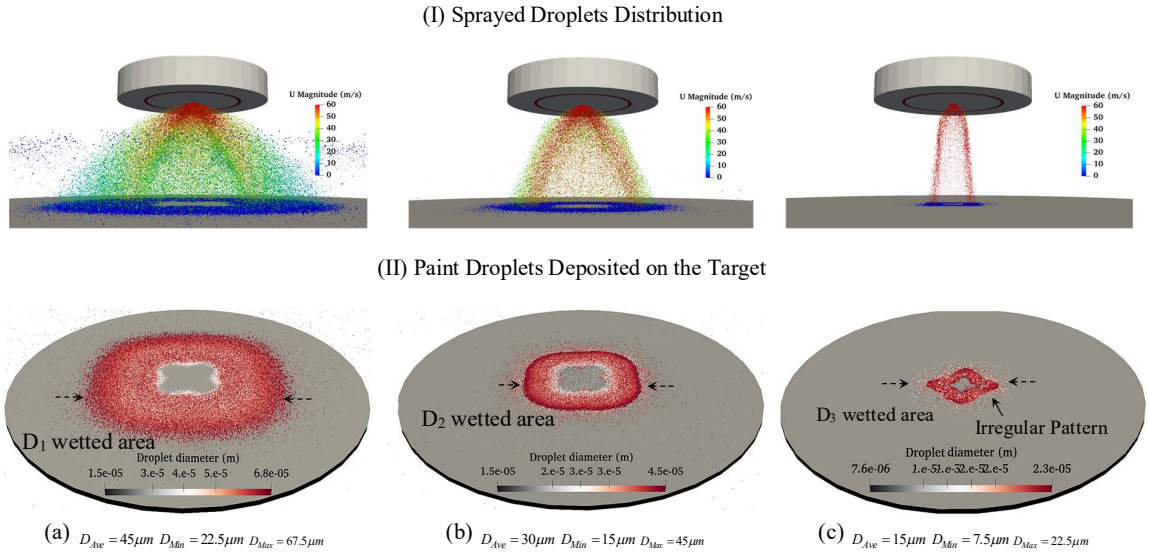

Figure 6: Impact of Droplet Size Distribution on Trajectory and Deposition Patterns: (a) $D_{Average} = 60\ \mu\text{m}$, (b) $D_{Average} = 30\ \mu\text{m}$, and (c) $D_{Average} = 15\ \mu\text{m}$ ($T_{Nitrogen} = 393.15^{\circ} K$).

Figures 7 and 8 illustrate the influence of varying charge-to-mass ratios and applied voltage on the electric field and spraying performance. Both parameters have a similar effect on the behavior of the discrete flow. Balancing spray transfer efficiency (TE) and quality while optimizing energy and material usage is crucial when adjusting these variables. Higher voltage and charge values result in a narrower spray profile, reduced overspray, and a more uniform and dense deposition. In contrast, when the electric field is turned off, the spray pattern becomes irregular and thinner. As shown in Figure 8, a moderate range of voltage and charge produces a thicker, more uniform film at an optimal cost. This suggests that the Nitrotherm continuous phase combined with a moderate electric field significantly enhances the behavior of the discrete spray phase.

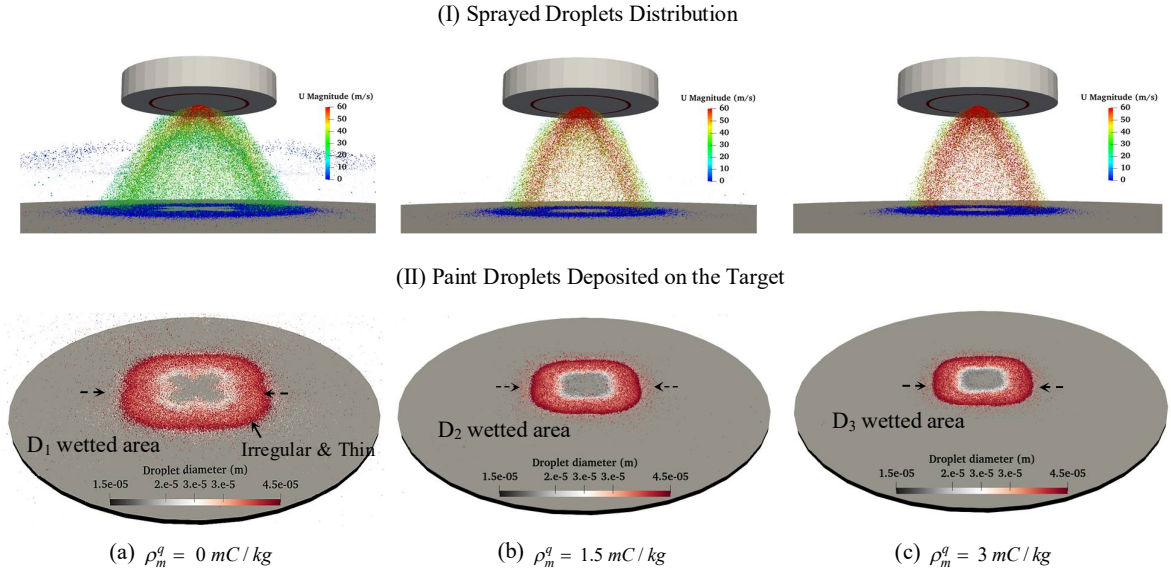

Figure 7: Impact of Charge-to-Mass Ratios (ρ_m^q) on spraying process: (a) $\rho_m^q = 0\ mC/kg$, (b) $\rho_m^q = 1.5\ mC/kg$, and (c) $\rho_m^q = 3\ mC/kg$ ($T_{Nitrogen} = 393.15^{\circ} K$).

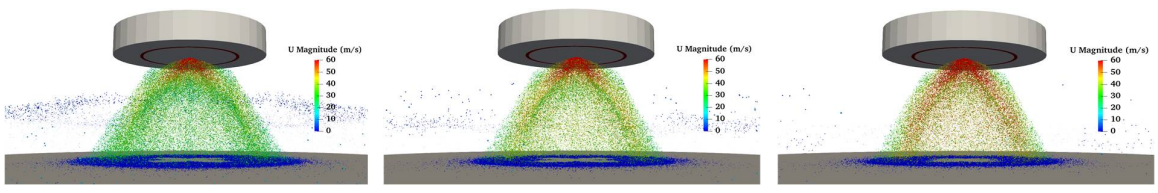

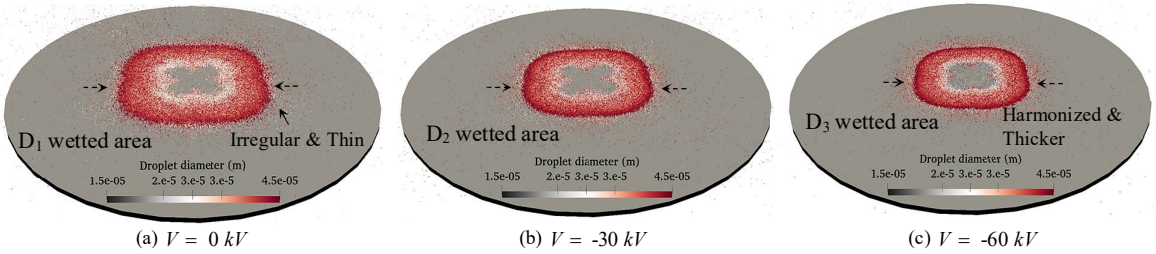

(a) $V = 0\ kV$ (b) $V = -30\ kV$ (c) $V = -60\ kV$

Figure 8: Effect of Applied Voltage on Droplet Trajectory and Deposition Pattern on Spraying Process: (a) $V = 0\ kV$,(b) $V = -30\ kV$, and (c) $V = -60\ kV$ ($T_{Nitrogen} = 393.15^{\circ} K$).

Figure 9 compares the effects of heated nitrogen (I) with compressed air (II). The results show that heated nitrogen enhances transfer efficiency (TE) and produces a more centralized, cosmetically appealing, denser, and thicker coverage. While temperature increases of nitrogen within a moderate range have minimal impact on trajectory and deposition pattern, very high temperatures lead to a reduction in droplet size in the central areas of the covered region, highlighting the efficiency of Nitrotherm spraying.

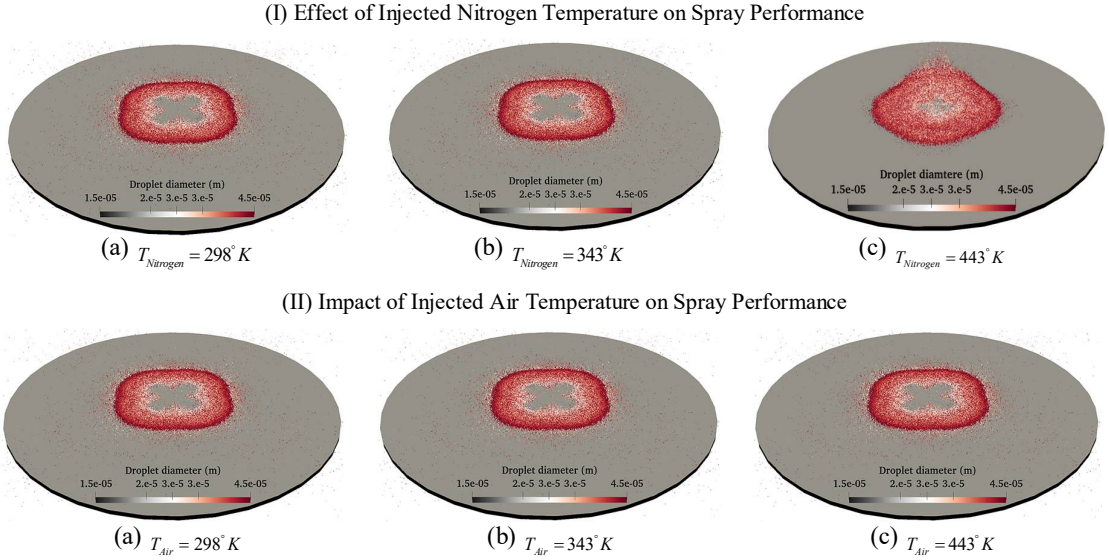

(a) $T_{Nitrogen} = 298^{\circ} K$ (b) $T_{Nitrogen} = 343^{\circ} K$ (c) $T_{Nitrogen} = 443^{\circ} K$

(a) $T_{Air} = 298^{\circ} K$ (b) $T_{Air} = 343^{\circ} K$ (c) $T_{Air} = 443^{\circ} K$

Figure 9: Comparison of the Effects of Heated Nitrogen (I) and Compressed Air (II) Injection on Droplet Deposition Patterns: (a) $T = 298.15^{\circ} K$, (b) $T = 343.15^{\circ} K$, and (c) $T = 443.15^{\circ} K$.

5 CONCLUSIONS

This study highlights the advantages of the Nitrotherm electrostatic spray technique, utilizing 3D Eulerian-Lagrangian simulations within the OpenFOAM framework. By solving the unsteady 3D compressible Navier-Stokes equations and employing a Large Eddy Simulation (LES) turbulence model, the research provides a detailed analysis of fluid dynamics and particle motion. The results indicate that optimizing nitrogen injection velocities and

droplet sizes significantly enhances film uniformity and reduces overspray. Furthermore, carefully calibrated electric field settings contribute to improved coating quality and efficiency. Compared to traditional air-based systems, the Nitrotherm technique provides superior performance with denser, more consistent coatings and environmental advantages.

AKNOWLEDGEMENT

This research was supported by the Project GreenAuto: Green Innovation for the Automotive Industry, n° 02/C05- i01.02/2022.PC644867037-00000013 from the Incentive System to Mobilizing Agendas for Business Innovation, funded by the Recovery and Resilience Plan. This research was also supported by the Portuguese Foundation for Science and Technology, I.P. (FCT, I.P.) FCT/MCTES through national funds (PIDDAC), under the R&D Unit C-MAST, Center for Mechanical and Aerospace Science and Technology, Research Unit No. 151, reference: Projects UIDB/00151/2020 (https://doi.org/10.54499/UIDB/00151/2020) and UIDP/00151/2020 (https://doi.org/10.54499/UIDP/00151/2020).

REFERENCES

[1] M. R. Pendar, F. Rodrigues, J.C. Páscoá and R. Lima, 2022. Review of coating and curing processes: Evaluation in automotive industry. Physics of Fluids, 34(10).

[2] Q. Ye, B. Shen, O. Tiedje, T. Bauernhansl, and J. Domnick. Numerical and experimental study of spray coating using air-assisted high pressure atomizers. *Atomization and Sprays*, 25(8):643–656, 2015.

[3] V. Viti and J. Kulkarni. CFD analysis of the electrostatic spray painting process with a rotating bell cup. In: *ILASS Americas, 21st Annual Conference on Liquid Atomization and Spray Systems*, Orlando, Florida, USA, 2008.

[4] P. J. O'Rourke and A. A. Amsden. A spray/wall interaction submodel for the KIVA-3 wall film model. *SAE Transactions*, pp. 281-298, 2000.

[5] A. Darwish Ahmad, A. M. Abubaker, A. A. Salaimeh, and N. K. Akafuah. Schlieren visualization of shaping air during operation of an electrostatic rotary bell sprayer: Impact of shaping air on droplet atomization and transport. *Coatings*, 8(8):279, 2018.

[6] C. Stevenin, Y. Bereaux, J. Y. Charmeau, and J. Balcaen. Shaping airflow characteristics of a high-speed rotary-bell sprayer for automotive painting processes. *Journal of Fluids Engineering*, 137(11):111304, 2015.

[7] M. R. Pendar and J. C. Páscoa. Numerical analysis of charged droplets size distribution in the electrostatic coating process: Effect of different operational conditions. *Physics of Fluids*, 33(3):033317, 2021.

[8] M. R. Pendar, S. Cândido, and J. C. Páscoa. Optimization of painting efficiency applying unique techniques of high-voltage conductors and nitrotherm spray: Developing deep learning models using computational fluid dynamics dataset. *Physics of Fluids*, 35(7), 2023.

[9] K. S. Im, M. C. Lai, S. T. J. Yu, and R. R. Matheson. Simulation of spray transfer processes

in electrostatic rotary bell sprayer. *Journal of Fluids Engineering*, 126:449-456, 2004. doi:10.1115/1.1758263.

[10] S. A. Colbert and R. A. Cairncross. A computer simulation for predicting electrostatic spray coating patterns. *Powder Technology*, 151:77-86, 2005. doi: 10.1016/j.powtec.2004.11.039.

[11] Q. Ye, T. Steigleder, A. Scheibe, and J. Domnick. Numerical simulation of the electrostatic powder coating process with a corona spray gun. *Journal of Electrostatics*, 54:189-205, 2002. doi:10.1016/S0304-3886(01)00181-4.

[12] V. Krisshna, W. Liu, and M. Owkes. High-fidelity simulations of a rotary bell atomizer with electrohydrodynamic effects. *International Journal of Multiphase Flow*, 168:104566, 2023.

[13] B. Shen, Q. Ye, N. Guettler, O. Tiedje, and J. Domnick. Primary breakup of a non-Newtonian liquid using a high-speed rotary bell atomizer for spray painting processes. *Journal of Coatings Technology and Research*, 16(6):1581–1596, 2019.

[14] A. Benmoussa, L. Rahmani, and B. Draoui. Simulation of Viscoplastic Flows in a rotating Vessel Using a Regularized Model. The International Journal of Multiphysics, 11(4), 349-358, 2017.

[15] L. Rahmani, O. Seghier, A. Benmoussa, and B. Draoui. CFD study of the thermal transfer of a non-Newtonian fluid within a tank mechanically stirred by an anchor-shaped impeller. In EPJ Web of Conferences, 180, p. 02089. EDP Sciences, 2018.

[16] W. Oswald, L. Geodeke, P. Ehrhard, and N. Willenbacher. Influence of the elongational flow resistance and pigmentation of coating fluids on high-speed rotary bell atomization. *Atomization and Sprays*, 29(10):913, 2019.

[17] P. Spang. Applying paints with nitrogen. *International Surface Technology*, 7(1):15, 2014.

[18] W. Bensalah, N. Loukil, M. Wery, and H. F. Ayedi. Assessment of automotive coatings used on different metallic substrates. *International Journal of Corrosion*, 838054, 2014.

[19] S. Ghosal. An analysis of numerical errors in large-eddy simulations of turbulence. *Journal of Computational Physics*, 125(1):187-206, 1996.

[20] M. R. Pendar and J. C. Páscoa. Study of the Plasma Actuator Effect on the Flow Characteristics of an Airfoil: An LES Investigation. *SAE International Journal of Advances and Current Practices in Mobility*, (2021-01-0016), pp.1206-1215, 2021.

[21] S. Laín and C. A. Grillo. Comparison of turbulent particle dispersion models in turbulent shear flows. *Brazilian Journal of Chemical Engineering*, 24:351-363, 2007.

[22] R. E. Bensow and C. Fureby. On the justification and extension of mixed methods. *Journal of Turbulence*, 8, 2007.

[23] M. R. Pendar and J. C. Páscoa. Atomization and spray characteristics around an ERBS using various operational models and conditions: numerical investigation. *International Journal of Heat and Mass Transfer,* 161, 120243, 2020.